Stronger net posterior cortical forces and asymmetric microtubule arrays produce simultaneous centration and rotation of the pronuclear complex in the early *Caenorhabditis elegans* embryo

Valerie C. Coffman[a], Matthew B. A. McDermott[b], Blerta Shtylla[c], and Adriana T. Dawes[a,d,*]
[a]Department of Molecular Genetics and [d]Department of Mathematics, The Ohio State University, Columbus, OH 43210; [b]Department of Mathematics, Harvey Mudd College, Claremont, CA 91711; [c]Mathematics Department, Pomona College, Claremont, CA 91711

ABSTRACT **Positioning of microtubule-organizing centers (MTOCs) incorporates biochemical and mechanical cues for proper alignment of the mitotic spindle and cell division site. Current experimental and theoretical studies in the early *Caenorhabditis elegans* embryo assume remarkable changes in the origin and polarity of forces acting on the MTOCs. These changes must occur over a few minutes, between initial centration and rotation of the pronuclear complex and entry into mitosis, and the models do not replicate in vivo timing of centration and rotation. Here we propose a model that incorporates asymmetry in the microtubule arrays generated by each MTOC, which we demonstrate with in vivo measurements, and a similar asymmetric force profile to that required for posterior-directed spindle displacement during mitosis. We find that these asymmetries are capable of and important for recapitulating the simultaneous centration and rotation of the pronuclear complex observed in vivo. The combination of theoretical and experimental evidence provided here offers a unified framework for the spatial organization and forces needed for pronuclear centration, rotation, and spindle displacement in the early *C. elegans* embryo.**

Monitoring Editor
Manuel Théry
CEA, Hopital Saint Louis

Received: Jun 16, 2016
Revised: Oct 3, 2016
Accepted: Oct 4, 2016

INTRODUCTION

Development of a multicellular organism relies on asymmetric cell division to differentiate specific cell types. Asymmetric cell division can occur in polarized cells, with the mitotic spindle positioned along the axis of polarization, causing the asymmetric inheritance of polarity determinants. Cell polarization in the *Caenorhabditis elegans* zygote depends on a conserved family of PAR proteins (partitioning defective). PAR proteins localize to the cortex of the single-celled embryo, establishing mutually exclusive anterior and posterior domains along the long axis of the embryo (Kemphues *et al.*, 1988; Etemad-Moghadam *et al.*, 1995; Guo and Kemphues, 1995; Watts *et al.*, 1996). The posterior domain is specified by the site of sperm entry during fertilization (Goldstein and Hird, 1996; O'Connell *et al.*, 2000; Wallenfang and Seydoux, 2000). The sperm contributes a pronucleus containing a haploid set of chromosomes and a centrosome or microtubule-organizing center (MTOC). The MTOC duplicates shortly after fertilization, and the two MTOCs move to opposite sides of the sperm pronucleus, with the MTOC axis (an imaginary line connecting the MTOCs) perpendicular to the long axis of the embryo (Gönczy *et al.*, 1999; DeSimone *et al.*, 2016). The MTOCs nucleate microtubule (MT) arrays, which are thought to be responsible for a striking sequence of mechanical events that reposition and reorient the pronuclei (Figure 1A). Specifically, the MT arrays first draw the female pronucleus to join the sperm pronucleus in the posterior of the embryo and then subsequently reorient the entire pronuclear complex (PNC, consisting of two MTOCs and two pronuclei) so that the MTOC axis is aligned with the polarity

This article was published online ahead of print in MBoC in Press (http://www.molbiolcell.org/cgi/doi/10.1091/mbc.E16-06-0430) on October 12, 2016.

*Address correspondence to: Adriana T. Dawes (dawes.33@osu.edu).

Abbreviations used: 2D, two-dimensional; EL, egg length; GFP, green fluorescent protein; MT, microtubule; MTOC, microtubule-organizing center; NEBD, nuclear envelope breakdown; PCM, pericentriolar material; PNC, pronuclear complex; ROI, region of interest.

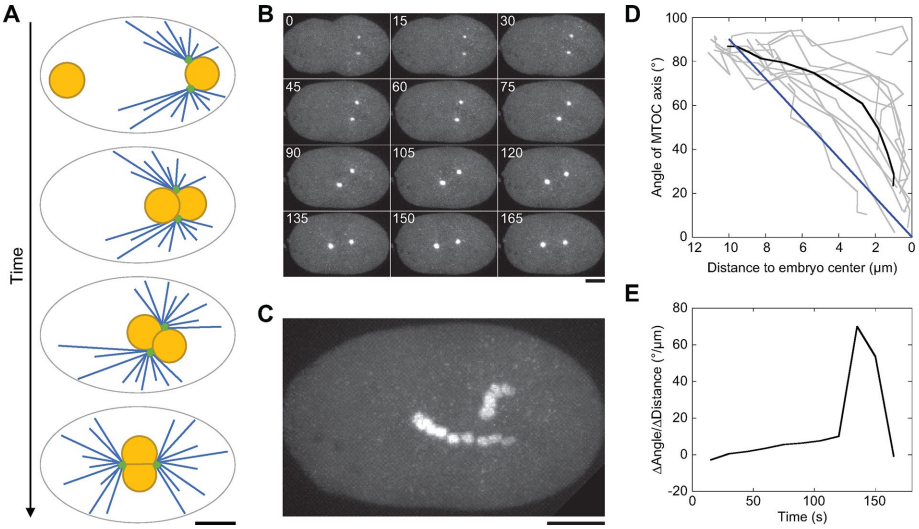

FIGURE 1: Pronuclear centration and rotation occur simultaneously between pronuclear meeting and NEBD. (A) Schematic of events before NEBD in the single-celled embryo (top to bottom): MTOCs (green) duplicate, mature, and nucleate MT arrays (blue); pronuclei (yellow) meet; entire complex rotates and centers; MTOC axis aligns with the long axis of the embryo. Anterior is at the left in this and all subsequent images. (B) EBP-2::GFP reveals MTOC positions during centration and rotation of the PNC. Time (s) is in the corner of each image. The pronuclei meet at time 0, and NEBD occurs at time 165. (C) A maximum-intensity projection through time of the embryo in B. Scale bars: 10 μm. (D) Graph of centration and rotation of the PNC in individual embryos (gray lines) and mean (black line, $n = 11$). The angle of the MTOC axis (*y*-axis) is time matched to the Euclidean distance of the PNC from the center of the embryo (*x*-axis) from pronuclear meeting to NEBD. The diagonal (blue line) lies below the majority of the curves. (E) Graph of the change in angle over the change in distance (*y*-axis) vs. time (*x*-axis) from polynomial curve fits of the data in D vs. time ($n = 10$; see *Materials and Methods*).

axis (Gönczy *et al.*, 1999). During this time, the PNC also moves to the center of the embryo. After nuclear envelope breakdown (NEBD), the spindle forms, and the astral MTs contribute again to a shift in location toward the posterior, reaching ~60% egg length (EL; Grill *et al.*, 2001, 2003; Labbé *et al.*, 2004). This final step creates the division asymmetry by specifying a division plane that leads to unequally sized daughter cells, with a corresponding asymmetric distribution of PAR proteins.

Microtubules, dynamic biopolymers nucleated in the MTOC (Mitchison and Kirschner, 1984), generate force by interacting either with cytoskeletal molecular motors or by using the energy of assembly and disassembly. Dynein is a minus end–directed molecular motor that is found both in the cytoplasm and on the cortex of *C. elegans* cells (Gönczy *et al.*, 1999; Hannak *et al.*, 2002). Dynein is enriched at the cortex, where it likely interacts with MTs from both MTOCs (Kotak *et al.*, 2012). When a dynein motor is attached to the cortex and also connects to an MT plus end, it can generate pulling force by attempting to walk toward the MT minus end. Indeed, pulling forces generated at the cortex have been proposed to be the dominant force-generating mechanism, as shown by laser-cutting experiments (Grill *et al.*, 2001, 2003). The nature of these pulling forces seems to be affected by cell polarity cues, since there is an imbalance in force-generating elements between the anterior and posterior end of a polarized cell (Grill *et al.*, 2001, 2003; Labbé *et al.*, 2004). In addition, MTs can generate pushing force through a Brownian ratchet mechanism, as demonstrated experimentally (Janson and Dogterom, 2004) and theoretically (Peskin *et al.*, 1993). For large cells such as the *C. elegans* embryo, cortical pulling forces can be sufficient to center the MTOCs, provided the number of cortical force generators is small compared with the number of MTs contacting the cortex: a "limited cortical force" assumption (Grill *et al.*, 2003; Grill and Hyman, 2005). Despite the importance of MT interactions with cortical force generators and their potential regulation by polarity determinants, it is not well understood how the PNC is repositioned in the early embryo (for review, see Dogterom *et al.*, 2005; Grill and Hyman, 2005).

At the boundary of the polarized PAR domains resides the Dishevelled, Egl-10, and Pleckstrin (DEP)–domain containing LET-99 protein (Rose and Kemphues, 1998; Tsou *et al.*, 2002). LET-99 localizes to a band around the cortex and is thought to inhibit dynein in that region (Rose and Kemphues, 1998). LET-99 activity in the posterior-lateral band is critical for the posterior shift of the spindle during mitosis (Rose and Kemphues, 1998; Krueger *et al.*, 2010). Knockdown of *let-99* produces a nuclear rocking phenotype during centration and rotation of the PNC, in which the MTOC axis wobbles back and forth as it rotates, and the PNC settles near 60% EL instead of centering. In the absence of LET-99, asymmetric division is similar to wild type, due to the incomplete centering of the PNC before NEBD (Rose and Kemphues, 1998).

Owing to the large number of components involved in PNC centration and rotation, mathematical modeling aligned with experimental data can help us better understand regulatory interactions between biochemical and mechanical components in the cell that are responsible for the observed PNC dynamics. Previous theoretical models of this system have focused on force-balance mechanisms that produce PNC centering due to forces that arise from interactions of MT arrays with uniformly distributed cytoplasmic dynein (Kimura and Onami, 2005; Kimura and Kimura, 2011; Shinar *et al.*, 2011). However, these prior models have been unable to recapitulate the smooth and well-timed rotation of the PNC. In these models, the PNC is assumed to be a perfect sphere that can reach the center of the ellipsoidal cell via an MT length–dependent cytoplasmic pulling force generated from symmetric MT arrays, but one study showed this mechanism is not sufficient to produce rotation of the PNC (Kimura and Onami, 2005). Stochastic symmetry breaking can initiate rotation but relies on MTs that grow almost tangentially to the sphere representing the pronuclei (Shinar *et al.*, 2011). One model produces partial rotation during centering by using spatial variation in cortical pulling forces representing the activity of LET-99, but this model relies on loss of LET-99 activity during mitosis for spindle displacement (Kimura and Onami, 2007).

In this work, we used complementary experimental and modeling approaches to demonstrate simultaneous centration and rotation of the PNC mediated by cortical dynein. Our mathematical model included zero pulling force in the posterior-lateral band and stronger net pulling forces in the very posterior than in the anterior. In addition, asymmetries in the nucleation angle of the MT arrays were sufficient to promote centration and rotation in the presence of these asymmetric cortical forces. Our novel model invokes similar physical properties to those observed during mitosis (Grill *et al.*, 2001, 2003; Labbé *et al.*, 2004) for proper centration and

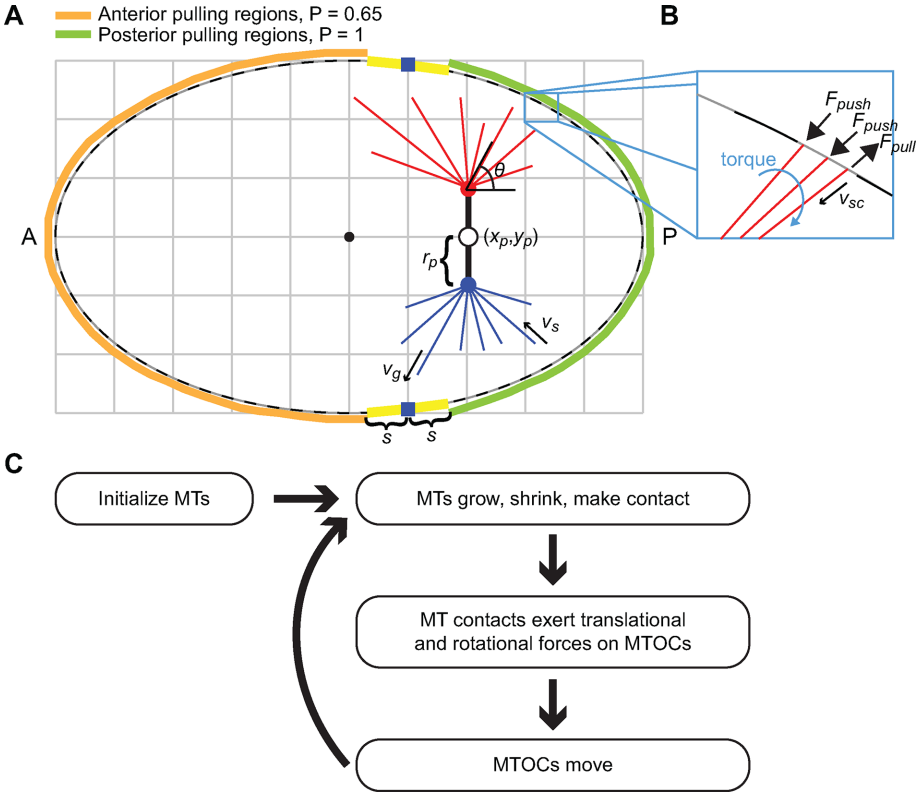

FIGURE 2: Overview of our 2D stochastic mathematical model. (A) Schematic of the components of the model in their initial configuration. A rigid rod centered at (x_p,y_p) (open circle) with respect to the center of the embryo (black point) is assumed to have two points from which rigid MTs nucleate (red and blue). Each MT can grow to contact the cortex and subsequently generate either pulling force (F_{pull}) or pushing force (F_{push}), depending on its cortical attachment position. The cortical band, centered on the cortex at 60% EL (blue square) extends in both directions symmetrically with arc length *s* (yellow bars). Different probabilities of pulling contacts exist to the left ($P = 0.65$, orange curved bar) and right ($P = 1$, green curved bar) of the cortical band. MTs experience dynamic instability with growth speed v_g and shortening speed v_s throughout the cytoplasm and catastrophe with speed v_{sc} after contact with the cortex (see the text for detailed model description). The 5 μm grid behind the embryo shows the scale. (B) Zoomed view of example MT contacts in one cortical region (see the text for description). (C) Flowchart showing sequence of model calculations at each time step.

rotation of the MTOCs before spindle formation, suggesting that a reversal of force asymmetries is not necessary before spindle displacement.

RESULTS

Pronuclear centration and rotation occur simultaneously

In *C. elegans* embryos expressing EBP-2::GFP (green fluorescent protein) from a transgene driven by the *pie-1* promoter, the male and female pronuclei met at 70 ± 2% EL from the anterior, similar to previous observations (Gönczy *et al.*, 1999; Kimura and Kimura, 2011). The pronuclei met 2.9 ± 0.2 min before NEBD ($n = 10$). The MTOC axis was 86.1 ± 5.3° from the long axis of the embryo when the pronuclei met, and in 10 out of 11 embryos it rotated at least 50° before NEBD (Figure 1, B–D). In some embryos, the angle at pronuclear meeting was >90° from where it ended, suggesting that the starting angle does not dictate the direction of rotation. In 10 embryos, the center of the PNC came within 1 μm of the center of the cell before NEBD, whereas one reached 2.5 μm from the center (Figure 1D). In the majority of observations, centration occurred slightly faster than rotation, as indicated by individual traces remaining above the line from (10 μm, 90°) to (0 μm, 0°) (Figure 1D, blue line). Below we used these observations to find appropriate parameters for our mathematical model. The shape of the plot of change in angle over change in distance from Figure 1D yielded additional criteria for validating the model (Figure 1E): that is, model results that yielded different shapes were assumed to be missing key features. Together these data demonstrate the simultaneous centration and rotation of the PNC, which has not been recapitulated by any previous mathematical models (Kimura and Onami, 2005, 2007; Kimura and Kimura, 2011; Shinar *et al.*, 2011).

Cortical dynein and symmetric MT arrays are sufficient to center but not rotate the PNC

Using a two-dimensional (2D) stochastic mechanical model, we simulated pronuclear dynamics from a starting position of 70% EL, corresponding to pronuclear meeting, until arrival of the PNC at the center of the cell, corresponding to NEBD. The mathematical model incorporated MT growth and shortening dynamics and pulling forces that arise from uniformly distributed regions on the cortex (Figure 2A; see *Materials and Methods* for details). All parameter ranges are given in Table 1. Similar to previous mathematical models of pronuclear dynamics, we implemented our model in a 2D geometry representing a midplane section of the early *C. elegans* embryo (Figure 2A). In contrast to previous models, we assumed the forces acting to center and rotate the embryo had the same spatial organization as the forces acting on the mitotic spindle (Grill *et al.*, 2001, 2003; Labbé *et al.*, 2004; Krueger *et al.*, 2010), since these events are separated in vivo by only a few minutes.

The MTOCs were represented by two points at the ends of a rigid rod with length $2r_p$ and center of mass located at (x_p, y_p), all of which represented the PNC in our model. Each MTOC (red = MTOC1 and blue = MTOC2, in Figure 2A), nucleated a fixed number of MTs (N_{MTi}, $i = 1, 2$) within a fixed nucleation angle span (*arrayRangei*, $i = 1, 2$). An individual MT was nucleated at angle θ, randomly chosen within the span with a uniform probability distribution. MTs grew with rate v_g, depolymerized with rate v_s, and stochastically transitioned between growing and shortening states with frequencies k_r (rescue) and k_c (catastrophe).

At the cortex, there were 128 regions (Figure 2A, alternating gray and black) in which a single MT at a time had a probability, $P > 0$, to make contact with a single dynein anywhere inside the region (Figure 2, A and B), consistent with a previous study (Grill *et al.*, 2003). If an MT reached a cortical region where there was no dynein available for attachment, then the MT was allowed to grow against the cortex and produce a pushing force, due to ratcheting of the growing MT against the cortical barrier. Thus the first MT that made contact at the cortex applied a dynein pulling force, F_{pull}, in the same direction of MT growth for a duration of C_{pull}, and any additional MT contacts in the same region applied a pushing force, F_{push}, in the opposite direction

Parameter	Parameter description	Simulation parameters[a]	Parameter search range	Reported range
Embryo dimensions				
L (μm)	Long axis	50		
W (μm)	Short axis	30		
r_p (μm)	Pronucleus radius	4		—[b]
Microtubules				
N_{MT1}	Number of MTs in MTOC1[c]	1284	675–2025	1500[d]
N_{MT2}	Number of MTs in MTOC2	1000		
v_g (μm/s)	Growth velocity[c]	0.73469	0.25–0.75	0.1–1[e,f,g,h]
v_s (μm/s)	Shrinkage velocity[c]	0.16361	0.13–0.4	0.1–0.8[e,g]
v_{sc} (μm/s)	Shrinkage velocity after contact[c]	2.59670	1–3	—[i]
k_c (s^{-1})	Cytoplasm catastrophe frequency[c]	0.03533	0.02–0.05	0.01–0.046[j]
k_r (s^{-1})	Cytoplasm rescue frequency[c]	0.06286	0.05–0.15	0.01–0.13[j]
arrayRange1 (°)	Size of MTOC1 array[c]	133	68–202	—[i]
arrayRange2 (°)	Size of MTOC2 array	120		—[i]
P_a	Probability of contact with dynein at anterior	0.65		—[i]
P_p	Probability of contact with dynein at posterior	1		—[i]
Forces				
F_{pull} (pN)	Cortical pulling force per MT[c]	0.82545	0.5–1.5	0.7–1.1[k,l]
F_{push} (pN)	Cortical pushing force per MT[c]	0.44531	0.25–0.75	5–10[m,n]
C_{pull} (s)	Pulling time at cortex per MT[c]	4.0704	3–9	1–75[g,o,p]
C_{push} (s)	Pushing time at cortex per MT[c]	0.4656	0.24–0.6	—[i]
Cell properties				
R	Number of cortical pull contact regions	128		—[i]
B (%L)	Cortical band position	60		—[i]
s (μm)	Half cortical LET-99 band arc length[c]	3.73	0–24	—[i]
a (pNs/μm^2)	Viscosity of the cytosol	1		0.001–10[e,g,q]
η (pNs/μm)	Translational drag coefficient[c]	6.60540	4–13	—[i]
μ (pNs/μm)	Rotational drag coefficient[c]	532.28096	300–900	—[i]
Model-specific parameter				
τ (s)	Time step	0.00025		

[a]Values used in simulations for Figures 3, 4, and 6 and Supplemental Figures S6 and S7, unless otherwise specified; [b]DeSimone *et al.* (2016); [c]Varied in parameter search (see *Results* and *Materials and Methods* for more details); [d]Spiró *et al.* (2014); [e]Kimura and Onami (2005); [f]Srayko *et al.* (2005); [g]Kozlowski *et al.* (2007); [h]Kimura and Onami (2007); [i]this study; [j]Cassimeris *et al.* (1988); [k]Gross *et al.* (2000); [l]Mallik *et al.* (2004); [m]Dogterom and Yurke (1997); [n]Janson and Dogterom (2004); [o]Brunner and Nurse (2000); [p]Labbé *et al.* (2003); [q]Daniels *et al.* (2006).

TABLE 1: Simulation parameters and their ranges.

of MT growth for a duration of C_{push} (Figure 2B). After contact, the MTs shrank with rate $v_{sc} > v_s$, due to MT catastrophe (Laan *et al.*, 2012). The net sum of all forces exerted by the MT contacts with the cortex generated both centration and rotation of the MTOCs at each time step (summarized in Figure 2C). In some simulations, we also included a posterior-lateral cortical band that did not contain any pulling contacts, referred to as cortical bands, to represent the location and proposed function of LET-99 in the embryo (Tsou *et al.*, 2002). The cortical bands were centered at 60% EL (Figure 2A, blue squares) and could extend in both directions along the cell periphery, up to 24 μm (Figure 2A, yellow bars). At the beginning of the simulation, MTs were initialized within the *arrayRangei* at random lengths up to the embryo periphery, since MT arrays are already established at the time of pronuclear meeting (Hyman and White, 1987).

The PNC is a bilobate structure, with the MTOCs sitting in the cleft between the lobes (see Figure 1A). For simplicity, we did not explicitly model the pronuclear boundaries; however, we limited the range of nucleation angles available to each MTOC to prevent MT growth into the pronuclei (*arrayRangei*). Inside the cell, we expect that some MTs might grow in other directions not captured by our 2D model; however, we restricted our attention to capturing PNC centration and rotation within the plane and thus ignored potential three-dimensional effects. This 2D geometry should capture the key features of PNC movement observed by microscopy, since slight compression of the embryo due to the method of mounting usually constrains the PNC to planar rotation in the midplane of the embryo (Walston and Hardin, 2010).

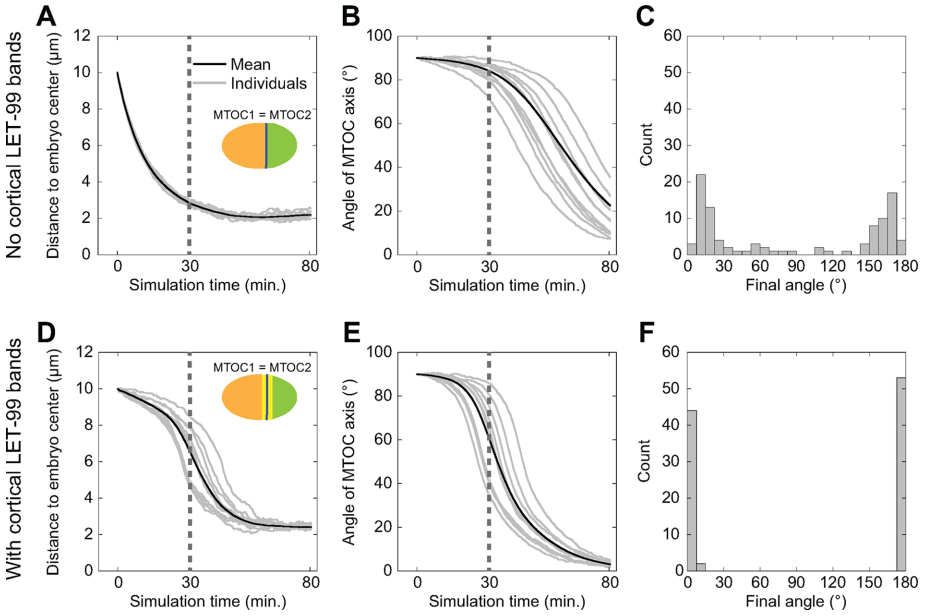

FIGURE 3: Simulations with and without cortical force asymmetry due to LET-99 produce centration and rotation. (A–C) Model with no LET-99 activity. (A) Graph of the Euclidean distance of the PNC from the center of the embryo over time in 10 individual simulations (gray) and mean (black, $n = 100$ runs) from the start of the simulation (time = 0) to the completion of centration and rotation to within ~20° of the long axis (time = 80). The dashed line at 30 min is a reference point for comparison with simulations in Figure 6. Inset, Schematic of cortical forces in these simulations: anterior (orange) and posterior (green) zones meet at 60% EL (blue line) with no band. The two MTOCs are equivalent in N_{MT} and *arrayRange* parameters. (B) Graph of PNC rotation in 10 individual simulations (gray) and mean (black, $n = 100$ runs). All angles are transformed to run from 90° (vertical) to 0° (horizontal). (C) Histogram of the final angle (at 80 min) of the MTOC axis ($n = 100$ runs). Unlike in B, the angles are not transformed. (D–F) Model including a region of LET-99 activity. (D) Graph of the Euclidean distance of the PNC from the center of the embryo over time in 10 individual simulations (gray) and mean (black, $n = 100$ runs). Inset, Schematic of cortical forces in these simulations: anterior (orange) and posterior (green) zones are separated by the cortical band (yellow) centered at 60% EL (blue line). The two MTOCs are equivalent in N_{MT} and *arrayRange* parameters. (E) Graph of PNC rotation in 10 individual simulations (gray) and mean (black, $n = 100$ runs). All angles are transformed to run from 90° (vertical) to 0° (horizontal). (F) Histogram of the final angle (at 80 min) of the MTOC axis ($n = 100$ runs). Unlike in E, the angles are not transformed.

We incorporated reported differences in cortical pull, with the posterior end of the cell having a stronger net pulling force compared with the anterior (Grill *et al.*, 2003; Labbé *et al.*, 2004), by altering the contact probabilities in the regions on either side of the bands (P_a and P_p, Table 1). Physically, we might interpret this as a difference in the ability of the MTs to connect to force generators or as a true difference in the amount of available dynein.

Using this model, we first considered simulations with symmetric MT arrays, each generating 1000 MTs with a nucleation angle range of 120°. The PNC centered before it rotated (Figure 3, A and B; see also Supplemental Video 1) and was equally likely to rotate in either direction (Figure 3C). These simulations demonstrate that cortical pulling forces were sufficient to center the PNC, similar to previous reports using length-dependent pulling forces by motor proteins assumed to be cytoplasmically anchored (Kimura and Onami, 2007; Shinar *et al.*, 2011). This is consistent with the PNC favoring locations where the total sum of cortical forces is zero, which happens at the geometric center of the ellipsoidal domain (Grill and Hyman, 2005; Kimura and Onami, 2007). In addition to the centering force, there is net torque exerted on the PNC due to stochastic MT interactions with the cortex. When the PNC was located at 70% EL and MTs from either array reached the cortex, they contacted more anterior cortical pull regions than posterior, since the posterior cortical region has higher curvature. This resulted in a net force on the PNC with a horizontal component pointing toward the geometric cell center. For symmetric MT arrays, the net torque on the PNC would be zero, since each array generates equal and opposing torque components corresponding to forces in the direction normal to the PNC axis. However, due to the stochastic nature of MT numbers binding on the cortex, rotational forces on the PNC axis did not balance for the two arrays, causing a persistent small net torque on the PNC. The orientation of the rotation was also driven purely by stochastic interactions of the MTs with the cortex, and in some cases the PNC rotated very little (<10%, equivalently 9°, from vertical) over periods of time much longer than the time required for centration (Figure 3, A–C). Overall this minimal model could not capture several features of PNC movement, with the most important being relative timing of centration and rotation. Thus additional factors were considered.

Cortical LET-99 activity decreases rotation time but does not recapitulate experimentally observed behavior

LET-99 localizes to a band near the boundary between anterior and posterior PAR protein domains from ~50–75% EL (Tsou *et al.*, 2002). In our model, the cortical bands were defined as areas where no pulling contacts were allowed, meaning the probability of an MT making contact with dynein was set to $P = 0$. However, in confocal images, fluorescently labeled LET-99 localized to the cortex with a Gaussian distribution centered at 62 ± 4.4% EL (mean ± SD; $n = 6$; Supplemental Figure S1). This implementation of the band effect in the model might overestimate the activity of LET-99; therefore we centered the band at 60% EL and varied the size of the band such that the arc length, s (Table 1), specified each half of the band stretching in both directions from the band center along the periphery of the cell. The size of the band used in the model was smaller than 50–75% EL (Supplemental Figure S1B, blue bar) and was obtained in a parameter search to recapitulate experimentally observed behavior, discussed below. With the addition of cortical bands, rotation was faster, but centration was slower compared with the minimal model simulation (Figure 3, D and E; see also Supplemental Video 2). By the end of the simulation time, the PNC had rotated completely and was equally likely to rotate in either direction (Figure 3F). The cortical band induced a force asymmetry, resulting in net torque and faster rotation of the PNC. Specifically, stochastic MT–cortex interactions caused a slight rotation in the PNC, so that MTs contacting the band exerted force asymmetrically on the centrosomes and induced further rotation. The cortical band also acted to slow PNC centration when the PNC was initially placed posterior to the band. This resistance to centration was alleviated once the PNC began to rotate. The combined effect of increased torque and resistance to centration from the LET-99 band can account for the observed faster rotation of the PNC.

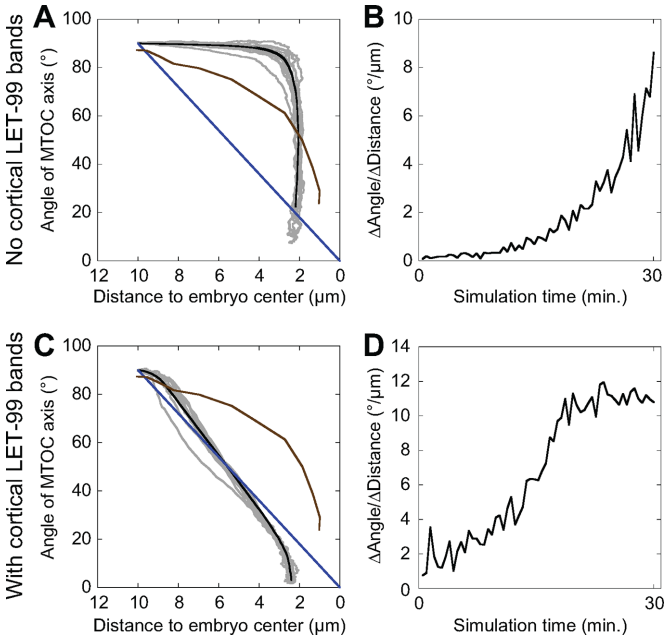

FIGURE 4: Simulations with or without LET-99 activity do not produce appropriate timing of centration and rotation. (A, B) Model with no LET-99 activity (same simulations as Figure 3, A–C). (A) Graph of centration and rotation of PNC in 10 individual simulations (gray lines) and mean (black line, $n = 100$). The angle of the MTOC axis (*y*-axis) is time matched to the Euclidean distance of the PNC from the center of the embryo (*x*-axis) from 0 to 80 min. The diagonal (blue line) is for comparison with Figure 1D. Mean data from Figure 1D are included (brown line). (B) Graph of the change in angle over the change in distance vs. time from mean simulation data in A. (C, D) Model including a region of LET-99 activity (same simulations as Figure 3, D–F). (C) Graph of centration and rotation of PNC in 10 individual simulations (gray lines) and mean (black line, $n = 100$). The angle of the MTOC axis (*y*-axis) is time matched to the Euclidean distance of the PNC from the center of the embryo (*x*-axis) from 0 to 80 min. The diagonal (blue line) is for compared with Figure 1D. Mean data from Figure 1D are included (brown line). (D) Graph of the change in angle over the change in distance vs. time from mean simulation data in C.

To determine whether our simulations with or without the LET-99 band recapitulated experimentally observed behaviors, we analyzed the shapes of curves comparable to Figure 1, D and E (Figure 4). For the simulations without LET-99 activity, although the curves remained above the diagonal line for most of the simulations (Figure 4A), the shape of the curve did not match experimental data (Figure 1D). When LET-99 activity was added, the curves dropped below the diagonal line (Figure 4C). None of the change in angle over change in distance plots was similar to experimental data (compare Figure 1E to Figure 4, B and D). The model with the LET-99 band incorporated all known sources of cortical asymmetry but did not recapitulate the experimental data. We hypothesized that another potential source of asymmetry might arise from the MT arrays nucleated by the MTOCs.

The MTOC that leads pronuclear rotation nucleates more microtubules in a larger array in vivo

We examined the following possible sources of MT array asymmetry: 1) the density of MTs nucleated at each MTOC might be different, and 2) the angles at which MTs grow from each MTOC might be limited by the pronuclear boundary to a different degree. Either of these sources of asymmetry might be able to speed up the rotation and would likely dictate which MTOC moves toward the anterior (hereafter referred to as the leading MTOC, whereas the MTOC that remains near the posterior is referred to as the lagging MTOC). For investigating MT array asymmetry, time-lapse images of embryos expressing GFP::TBB-2 (β-tubulin) or EBP-2::GFP (EB-1–like protein) label growing MT tips (Srayko *et al.*, 2005), were oriented so that the leading and lagging MTOCs could be analyzed separately, shown schematically in Figure 5A. Examination of embryos expressing GFP::TBB-2 revealed a difference in the angle of nucleation within the MT arrays (Figure 5, B and C). We quantified this difference throughout the centration and rotation period in embryos expressing EBP-2::GFP so that only growing MTs were included in our analysis. The analysis consisted of using an algorithm to find the edges of the MT arrays (see *Materials and Methods* for details) and then measuring the angle of the array with the vertex positioned at the centrosome and the arms of the angle including all of the signal. Indeed, the pronuclear boundary constrained the range of angles at which MTs could grow, and leading MTOCs had a significantly larger span of MT nucleation angles throughout the centration and rotation event (Figure 5, D and E). We determined significance using a standard linear statistical model that takes into account both time and group membership (lagging or leading MTOC). Both time and group were significant factors for the nucleation angle (Figure 5E), meaning there was a significant difference in the angle of MT nucleation between the lagging and leading MTOCs and that significant changes in the nucleation angle occurred over time. In contrast, only group was significant for EBP-2::GFP intensity (Figure 5F), indicating that the density of actively growing MTs was significantly different between the leading and lagging MTOCs, but the density did not significantly vary over time. Thus, in addition to nucleating a broader array of MTs, the leading MTOCs exhibited a higher density of EBP-2::GFP, and thus growing MTs, in the array (Figure 5F). In contrast, the intensity of EBP-2::GFP in the leading and lagging MTOCs, likely representing many very short MTs at the MTOC (Srayko *et al.*, 2005), was not significantly different (Supplemental Figure S2B). Together these data show that the leading MTOC nucleated more MTs over a wider range of angles compared with the lagging MTOC.

Simulations with asymmetric MT arrays and cortical LET-99 bands recapitulate experimentally observed centration and rotation dynamics

To simulate the asymmetry in the MT arrays, we modified the range for the angle of nucleation of MTs, to 133° for MTOC1, keeping MTOC2 at 120°, consistent with our measured angles. We also increased the MT number for MTOC1 relative to MTOC2, which produces a greater MT density on MTOC1, consistent with our measurements. Under these conditions, the centration started slightly faster than rotation, and rotation was completed within the time it took to center the PNC (Figure 6A; see also Supplemental Video 3). The curve remained above the diagonal throughout the simulation, similar to experimental data (compare Figure 6A with Figure 1D). The change in angle over change in distance graph also resembled that of experimental data (compare Figure 6B with Figure 1E). In addition, the trajectories of the MTOCs closely followed experimental trajectories (Figure 6, C and D). Notably, although the rotation in previous versions of our model had an equal probability to go in either direction (Figure 3, C and F), asymmetry in the MT array dictated which MTOC was the leading MTOC (Figure 6E), so the MTOC with the larger array went to the anterior in 100% of the simulations, consistent with experiments (Figure 5, A and B). These data show that the MT array asymmetry promoted rotation during centration with similar relative timing to experimental data.

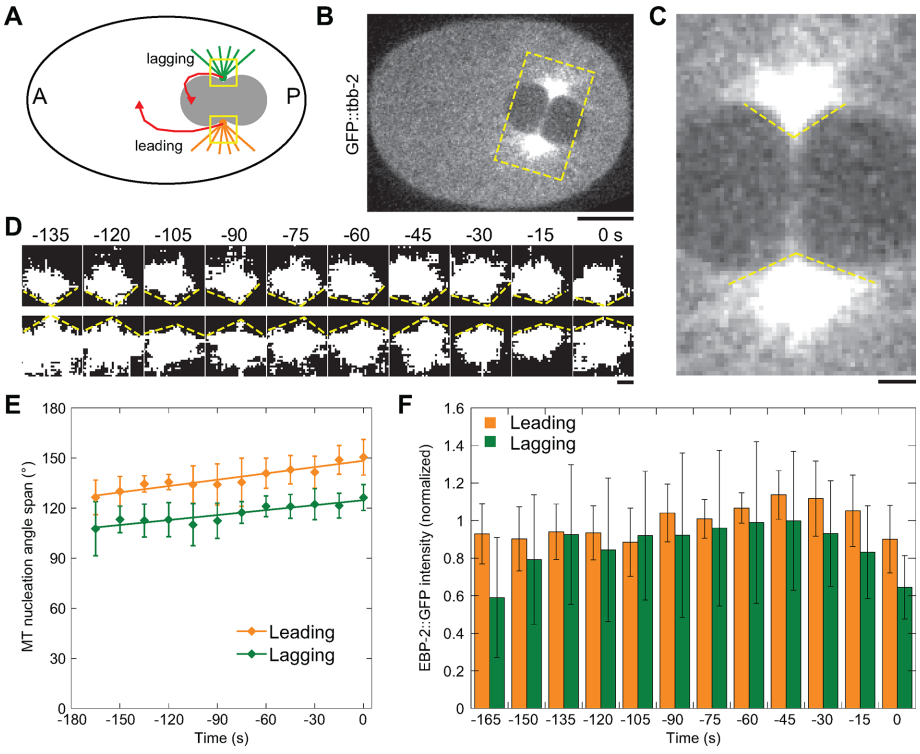

FIGURE 5: The MTOC that leads pronuclear rotation has a larger, denser MT array. (A) Schematic of the *C. elegans* embryo at pronuclear meeting showing the orientation of the images in D (yellow boxes). (B) Single-plane image of an embryo expressing GFP::TBB-2 just after rotation has begun. Scale bar: 10 μm. (C) Same image as in B, rotated and cropped with the leading centrosome on the bottom. Approximate array angles are marked (dashed yellow lines). Scale bar: 2 μm. (D) Thresholded images of EBP-2::GFP signal after implementation of an edge-preserving rolling average (see *Materials and Methods*). Dashed yellow lines indicate the nucleation angle span as measured. Time 0 is at NEBD. Scale bar: 2 μm. (E) Graph of nucleation angle span measurements from the time of pronuclear meeting until NEBD (time 0), $n = 11$. Error bars represent SD, and linear curve fits are included. (F) EBP-2::GFP intensity from leading and lagging MT arrays normalized to the time-averaged leading MTOC value for each embryo (see *Materials and Methods*).

Statistical analysis indicates LET-99 band size and MT nucleation angle are critical for recapitulating in vivo behaviors

We conducted a comprehensive search of parameter space to determine which parameters were driving certain model behaviors, such as simultaneous centration and rotation. We found that parameters associated with both cortical and centrosomal asymmetries, in particular the size of the LET-99 band and the MT nucleation angle, were constrained when we required the model to recapitulate experimentally observed behaviors (Supplemental Figures S3 and S4) and had statistically significant effects on model behaviors (Supplemental Figures S5–S7). In addition, we found that increasing the pulling force of dynein decreased the amount of time needed to center and rotate the PNC (Supplemental Figure S4, A–C) due to the stronger forces inducing higher torque on the PNC. See the Supplemental Material for an in-depth discussion of the statistical analyses and corresponding results. This unbiased analysis of parameter space reinforces our findings that in vivo behaviors such as simultaneous centration and rotation are a robust property of the mathematical model and rely on a small number of key cortical and centrosomal features.

DISCUSSION

Using a combination of mathematical modeling and experimental data, we propose that dynein-mediated cortical pulling forces in combination with MT array asymmetries are sufficient to generate proper centration and rotation of the PNC in the early *C. elegans* embryo. With the addition of the LET-99 band, we have shown that, while the band is not necessary for centration and rotation, it might provide important temporal cues for PNC dynamics. Indeed, LET-99 appearance is tightly connected with cortical polarization cues (Tsou *et al.*, 2002). Thus it is appealing to hypothesize that this band might speed up rotation once the establishment of cortical polarity is complete, similar to its role in the posterior (P1) cell at the two-cell stage (Tsou *et al.*, 2003). Further, we have shown that cortical pulling and pushing forces in combination with asymmetric MT arrays allow us to obtain correct positioning of the PNC by offsetting stronger posterior pulling forces with a larger MT array contacting the anterior cortex. We note that the larger anterior MT array, which will likely adopt a very similar configuration as the posterior array after NEBD, might explain the source of the transient anterior tether, proposed by Labbé *et al.* (2004) to offset stronger posterior forces.

Our mathematical model diverges from previous models in several key respects. 1) We use cortical dynein activity. In previous models of pronuclear rotation, dynein activity was cytoplasmic, and net force therefore depended on MT length (Kimura and Onami, 2005; Shinar *et al.*, 2011). One drawback to this mechanism is that dynein anchored to large cargo is required to be uniformly distributed in the embryo cytoplasm; however, a more random organelle distribution of varying sizes is more likely, which would introduce significant stochasticity in force generation. Further, cytoplasmic flows might impact this localization assumption in nontrivial ways. 2) The spatial distribution of cortical force generation in our model is similar to previous models of spindle displacement that use cortical dynein (Grill *et al.*, 2001, 2003; Kimura and Onami, 2007), whereas previous models of PNC dynamics either did not incorporate any force asymmetry (Kimura and Onami, 2005; Shinar *et al.*, 2011) or assumed a reverse spatial profile (Kimura and Onami, 2007). Because pronuclear rotation and spindle formation occur within a few minutes in the embryo (Labbé *et al.*, 2003), it is simpler to assume that force-generating mechanisms may be similar. 3) We limit the amount of dynein available to move the pronucleus by allowing one contact at a time in each of 128 cortical regions. Owing to the limits we place on the size of the MT arrays, approximately one-third of the cortical regions are accessible to the MT arrays at any time. This is consistent with MTOC disintegration experiments showing that the amount of dynein is limiting (Grill *et al.*, 2003). Models using cytoplasmic length-dependent dynein forces do not have such limitations. 4) We use a small region of zero dynein activity to represent the activity of LET-99. The distribution of LET-99 is approximately Gaussian, centered around 60% EL (Supplemental Figure S1), and we let the model output dictate the optimal size of this band. In a previous model that included LET-99 regulation of dynein activity, the shape of the

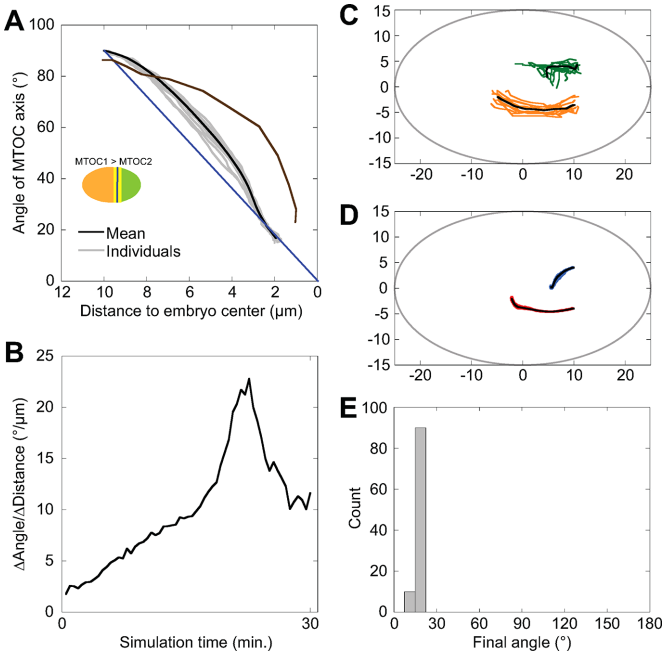

FIGURE 6: Simulations with a posterior-lateral band and MT array asymmetry produce appropriate relative timing of centration and rotation. (A) Graph of centration and rotation of the PNC in 10 individual simulations (gray lines) and mean (black line, $n = 100$ runs). The angle of the MTOC axis (*y*-axis) is time matched to the Euclidean distance of the PNC from the center of the embryo (*x*-axis) from the beginning of the simulation (time = 0) to the time the PNC reaches the center (time = 30 min). The diagonal (blue line) is for comparison with Figure 1D. Mean data from Figure 1D are included (brown line). Inset, Schematic of cortical forces in these simulations: anterior (orange) and posterior (green) zones are separated by the cortical band (yellow) centered at 60% EL (blue line). The two MTOCs are not equivalent, with $N_{MT1} > N_{MT2}$ and *arrayRange1* > *arrayRange2*. (B) Graph of the change in angle over the change in distance vs. time from mean simulation data in A from the start of the simulation until the PNC reaches the center. (C) Graph of individual MTOC trajectories, anterior (orange) and posterior (green), from time-lapse microscopy of EBP-2::GFP (mean traces in black), scaled to the embryo size (gray ellipse). (D) Graph of individual MTOC trajectories, anterior (red) and posterior (blue), and mean trajectories (black, $n =$ 100 runs) from simulations, scaled to the embryo size (gray ellipse). (E) Histogram of the final angle (at 30 min) of the MTOC axis when MT arrays are asymmetric ($n = 100$ runs).

repression was non-Gaussian (Kimura and Onami, 2007). 5) We incorporate novel MT array asymmetry and a limitation on the range of nucleation angles as measured in vivo (see below). Previous models have used symmetric arrays with at least a 180° nucleation range (Kimura and Onami, 2005, 2007; Shinar *et al.*, 2011). These new features allow our model to recapitulate the consistent timing and smoothness of experimentally observed pronuclear rotation.

Experimentally, we found a novel asymmetry in MT arrays nucleated from the two MTOCs that correlates with their final orientation after pronuclear rotation. This asymmetry predicts the direction of rotation in our model and might arise from several possible mechanisms that are not mutually exclusive. 1) The nucleation capacity of the two MTOCs might differ based on asymmetric recruitment of γ-tubulin. In the *C. elegans* zygote, the MTOC contributed by the sperm duplicates and matures by adding pericentriolar material (PCM), including γ-tubulin, before the pronuclear meeting (Marumoto *et al.*, 2005; Bettencourt-Dias *et al.*, 2011). The size of the MTOCs is limited by maternally supplied SPD-2 (Decker *et al.*, 2011), but the amount of γ-tubulin recruited correlates with the amount of SAS-4 at the centriole in RNA interference experiments (Kirkham *et al.*, 2003). A mathematical model of MTOC maturation demonstrates how two similar-sized MTOCs can form in a single cell from one cellular pool of components (Zwicker *et al.*, 2014). These data have been interpreted to mean that the two MTOCs are exactly equal in size and recruitment of PCM components, but they do not rule out the possibility that subtle differences exist. Indeed, we show here that the differences need not be large to produce the asymmetry in observed MT numbers (Figure 5C). The computational model also suggests small asymmetries in the MT nucleation angle are sufficient to bias the rotation of the PNC (Supplemental Figures S4E and S7A). 2) The stochastic recruitment of PCM to differing degrees might also affect the overall size of the MTOC, resulting in positional differences with reference to the bilobate PNC. The MTOCs sit in the cleft between the pronuclei throughout rotation, but a smaller MTOC might move deeper into the cleft, limiting the angle of nucleation, as seen with the lagging MTOC (Figure 5B). 3) A difference in the anchoring of the two MTOCs to the nuclear envelope might also affect the nucleation range of the arrays in a similar manner. The nucleation angles in our model might represent differences in MTOC attachment to the nuclear envelope via ZYG-12, which localizes throughout the outer nuclear membrane and the MTOC (Malone *et al.*, 2003; Minn *et al.*, 2009). An MTOC that is less tightly associated with the nuclear envelope might be free to leave the cleft slightly in order to promote a larger MT array.

The presence of LET-99 is not necessary to generate centration and rotation in vivo. However, the absence of LET-99 can cause MTOCs to move faster, as the PNC rocks while it rotates (Rose and Kemphues, 1998; Tsou *et al.*, 2002). Thus the activity of LET-99 is described as inhibition of force generation (Tsou *et al.*, 2002). Although our model suggests the LET-99 bands are important for generating consistent and appropriate relative timing of centration and rotation, we do not see nuclear rocking when we remove the LET-99 band from our model (Figure 3B). It is also unclear how inhibition of force generation by cortical LET-99 could lead to its role in promoting spindle rocking (Tsou *et al.*, 2002). These data suggest that the function of LET-99 is more complex than previously assumed.

Owing to the presence of many elements changing stochastically and interacting in the model, it was important to study the effects that various parameters had on model behavior. For this purpose, we implemented extensive and systematic parameter searches and uncovered important parameters needed to create the observed PNC dynamics. Specifically, the correlation analysis indicated that the size of the LET-99 band is important for model outcomes, with a small band needed to prevent large *y* excursions of the PNC. More broadly, important parameters are related to dynein activity, MT array asymmetry, and LET-99 band size. This indicates that both cortical force cues and MT array asymmetries are necessary to generate the correct model behavior. On the basis of the correlation analysis, we focused on model sensitivity to variations in LET-99 band size and MT array sizes individually (Supplemental Figures S6 and S7 and Supplemental Video 4). For the band sizes, we discovered a maximal band threshold that causes failure in rotation (Supplemental Figure S6). This indicates that potential perturbations in PAR signaling causing LET-99 regions to expand can seriously impact PNC dynamics. Further, changes in MT array size showed that centration and rotation can be robust to variations in MT array asymmetry, because final PNC positions did not vary significantly as one MT array increased in

size (Supplemental Figure S7B). This behavior is most likely related to the limiting cortical pulling-point assumption (Grill and Hyman, 2005), which reduces the sensitivity of the model to variations in MT numbers. These model results suggest two experimentally testable hypotheses. First, the model suggests that decreasing the spatial extent or eliminating the LET-99 band altogether without perturbing the localization of other cortical factors should result in faster centration compared with rotation, with the PNC able to make larger excursions away from the polarity axis and more variable timing of the initiation of rotation. Second, loss of asymmetry in the MT array should also lead to faster centration followed by slow rotation of the PNC, a feature predicted by earlier models (Kimura and Onami, 2005; Shinar *et al.*, 2011).

Our model, with both cortical and MT array asymmetries, implicitly addresses the issue of anterior to posterior pulling force differences. In the Kimura and Onami (2007) model, this cortical pulling force asymmetry was proposed to be corrected by the introduction of the LET-99 band. However, they did not carefully track rotation dynamics, and in our model, the size of the LET-99 band can significantly affect PNC rotation. Indeed, we propose that the role of the LET-99 band is to speed up the timing of rotation, but the bands are not needed to center or rotate the PNC. Our MT array asymmetry also likely explains the data from Labbé *et al.* (2004), who proposed that more anterior pulling force contacts might exist before NEBD, resulting in a larger anterior-directed force. Simulations of our model indicate the final *x* position of the PNC is highly stable near the center of the cell. To account for the posteriorward movement of the PNC after NEBD, we postulate that loss of the pronuclear membrane allows for a large and symmetric MT nucleation angle at both MTOCs. Preliminary trials with our model show a posterior displacement (unpublished data) corresponding to the observed spindle positioning during metaphase and anaphase, when we use symmetric MT arrays with a nucleation angle of 180° and initialize the MTOCs at the center aligned along the long axis of the cell.

In this study, we tested a mechanism for PNC centration and rotation arising solely from cortical force-generating elements. This assumption is supported by previous work on spindle positioning (Grill *et al.*, 2003; Labbé *et al.*, 2004; Kimura and Onami, 2007; Kotak *et al.*, 2012). We do not rule out the role of cytoplasmic dynein as a length-dependent centering force on the PNC; however, we have shown here that cortical forces are sufficient to produce the well-timed centration and rotation of the PNC. We expect that cytoplasmic dynein forces would shorten the time to centration and possibly disturb the relative timing between rotation and centration we have seen here. Further, we have not incorporated other important elements that may affect PNC dynamics. For instance, cytoplasmic streaming likely affects both PNC centration and rotation. In our model, we can match the relative timing of centration and rotation, but the overall time to finish is still longer than experimental observations. Future work will expand this model to better replicate the overall timing of the PNC centration and rotation process. In conclusion, this study illustrates how a cortically driven mechanism, relying on asymmetry of the MT arrays and dynein pulling forces, can generate the key features of PNC centration and rotation dynamics.

MATERIALS AND METHODS

Nematode strains and genetic methods

The MAS37 (abcIs3 [pie-1p::ebp-2::GFP + unc-119(+)]) and WH204 (ojIs1 [pie-1p::GFP::tbb-2 + unc-119(+)]) strains were provided by the Caenorhabditis Genetics Center (Minneapolis, MN), which is funded by the National Institutes of Health (NIH) Office of Research Infrastructure Programs (P40 OD010440). The TH73 strain (unc-119(ed3)III; ddIs64[pie-1p::YFP::let-99(genomic);unc-119(+)]) was a gift from Henrik Bringmann (Bringmann *et al.*, 2007). Strains were maintained on nematode growth media agar plates seeded with OP50 *Escherichia coli* as a food source. Strain stocks were maintained at 20°C by chunking or picking wild-type worms as needed and were stored at −80°C according to standard practices.

Microscopy and image analysis

Microscopy images were taken using a 60×/1.4 NA Plan-Apo objective lens (Nikon, Melville, NY) on a spinning-disk confocal microscope (UltraVIEW Vox CSUX1 system; PerkinElmer, Waltham, MA) with 440-, 488-, 515-, and 561-nm solid-state lasers and a back-thinned EMCCD camera (Hamamatsu Photonics, Bridgewater, NJ) on a Ti-E inverted microscope (Nikon) without binning. Gravid hermaphrodite worms were transferred to a coverslip with egg salts buffer (118 mM NaCl, 48 mM KCl, 2 mM $MgCl_2$, 2 mM $CaCl_2$, 0.025 mM HEPES, pH 7.4) and dissected to release embryos. Coverslips were then inverted onto slides with 2% agar pads (in egg salts buffer) and sealed with Petrolatum (S80117; Fisher, Waltham, MA). Time-lapse z-stacks were taken with 1.5 µm spacing, spanning 30 µm centered at the midplane of the embryo, with a 15 s delay between stacks. Images were always collected until after the first division to ensure the embryos divided with normal timing, indicating that they were healthy.

Image analysis and maximum-intensity projections shown in the figures were made in ImageJ (NIH, Bethesda, MD). For Figure 1E, the analysis was as follows. For each embryo, MTOC angle versus time and distance from center versus time were plotted. Each plot was fitted with up to a third-degree polynomial function to smooth the data. The embryo in which the PNC did not rotate was excluded, because the curve fitting was poor. The change in angle over change in distance was calculated from the curve fits for each time point, then averaged over the remaining 10 embryos. The plot in Figure 1E is the average of the change in angle over change in distance for each time point. The shapes of this curve and that in Figure 1D were used to determine whether our mathematical model recapitulated experimentally observed behaviors.

For Figure 5 analysis, embryo images were rotated and flipped as necessary so that the anterior was at the left and the MTOC that went to the anterior started on the bottom. All images were then cropped to 50 µm × 30 µm for analysis of MTOC positions. Thresholded images of EBP-2::GFP were created by rotating all images so that the MTOC axis was vertical and cropping a 60 × 60 pixel region of interest (ROI) with the MTOC positioned at (30, 40) for posterior and (30, 20) for anterior MTOCs. An edge-preserving rolling average (modified Chung-Kennedy algorithm) was applied horizontally and vertically to each ROI, similar to the method used to determine the intensity of a single GFP molecule in photobleaching quantification experiments (Leake *et al.*, 2006; Engel *et al.*, 2009; Coffman *et al.*, 2011). Briefly, the SDs of intensities in two consecutive groups of three pixels were compared, and the mean of the group with lower SD was used in the output. Groups with higher SDs are assumed to cross boundaries. Thus the algorithm distinguishes signal from nonsignal and sharpens the boundary between them. Each iteration of the algorithm resulted in a loss of 5 pixels but improved the contrast between background and EB-1 intensity in the nucleation region by finding the edge of the intensity. The horizontal and vertical filtered images were then cropped to 45 × 45 pixel squares and averaged to get the final images used to measure the nucleation angles. The resulting image is nearly binary, showing regions with signal (white) and regions without (black). A threshold was

applied to these figures to make them binary, with all signal appearing as the same shade of white (Figure 5D).

The intensity of EBP-2::GFP within the MT nucleation region (Figure 5F) was determined by drawing a rectangular ROI the size of the PNC and including the very bright MTOC region at each time point in the best focal plane. The MTOC was cropped out of the intensity measurement and then nuclear intensity was subtracted as the background (Supplemental Figure S2A). The time-averaged intensity of the anterior nucleation region was normalized to 1 for each embryo. The average normalized intensity at each time point was plotted (mean ± SD). MTOC intensities removed from the above measurement, with nuclear background subtracted, were also normalized based on the time-averaged anterior intensity in each embryo (Supplemental Figure S2B). Because this is a transgenic strain that also expresses native untagged EBP-2, we assumed that the tagged protein localized similarly to both arrays so that the intensity was representative of each array's density, relative to each other. We cannot obtain absolute numbers of MTs from this strain because of the presence of untagged protein, so the density was the closest approximation we could get.

The distribution of YFP::LET-99 in the embryo was determined from cortical imaging planes during the first mitosis, when the band was enriched over cytoplasmic background (Supplemental Figure S1), consistent with immunostaining (Tsou *et al.*, 2002). A rectangular ROI the size of the embryo at the midplane was drawn, and the intensity plot across the entire embryo was created. The curve was fitted with a fourth-degree polynomial function, and the derivative function was solved to find the local maximum nearest to 60% EL. The mean and SD of these values are reported in the text (62 ± 4.4% EL). The band was centered at 60% EL in our model for simplicity. The plot of YFP::LET-99 intensity was created by normalizing the *x*-axis values of the intensity profile of each embryo in terms of % EL, binning the values every 1% centered on integer values, and plotting a rolling average of these values to smooth the curve. Fluorescence intensity was normalized to the average curve minimum and maximum at 60% EL.

Mathematical model

We built a mathematical model of pronuclear centration and rotation that operated under the same conditions required for proper spindle positioning in the early embryo (Grill *et al.*, 2003; Grill and Hyman, 2005; Labbé *et al.*, 2004). That is, we assumed that dynein was evenly distributed on the cortex (Gönczy *et al.*, 1999; Hannak *et al.*, 2002); that dynein exerted the same pulling force, regardless of location; that the amount of dynein was limiting (Grill *et al.*, 2003; Grill and Hyman, 2005), so that not every MT contacting the cortex experienced a pulling force; and that there was a lower probability of an MT having a productive interaction with dynein in the anterior half of the cell compared with the posterior half. Those MTs not interacting with dynein can exert a pushing force on the cortex. The vector associated with the *j*th MT is denoted $\vec{F}_j^{MT} = \left(x_j^{MT} - x_p, y_j^{MT} - y_p\right)$, where (x_p, y_p) is the center of mass of the pronuclear rod.

We used the index $i = 1, 2$ to indicate each MTOC. The force applied by the *j*th MT on its MTOC is given by

$$\alpha\ \vec{e}_j = \alpha \frac{\vec{F}_j^{MT}}{\left|\vec{F}_j^{MT}\right|} \tag{1}$$

where $\vec{e}_j$ gives the orientation of each MT and $\alpha = F_{\text{pull}}, F_{\text{push}}$ corresponds to the magnitude of the force due to dynein pulling or polymerization pushing, respectively. The net force experienced by each MTOC is

$$\vec{F}_1 = \sum_{j=1}^{N_{MT1}} \vec{F}_j^{MT}, \quad \vec{F}_2 = \sum_{j=1}^{N_{MT2}} \vec{F}_j^{MT} \tag{2}$$

The movement of each pronuclear MTOC was governed by Langevin equations that describe movement in an overdamped (or friction-dominated) regime. Each MTOC had a net force due to the MTs that were connected to the cortex, which in turn was transmitted to the center of mass of the rod as follows:

$$\eta \frac{dx_p}{dt} = \vec{F}_{x,1} + \vec{F}_{x,2} + \psi_x(t), \text{translational motion in x direction} \tag{3}$$

$$\eta \frac{dy_p}{dt} = \vec{F}_{y,1} + \vec{F}_{y,2} + \psi_y(t), \text{ translational motion in y direction} \tag{4}$$

where η is the translational drag coefficient for the PNC and $\psi(t)$ represents a random force term. The magnitude of the random force was chosen so that the simulation results matched the experimental data. We envisioned that the random force term in our model equations included both simple thermal diffusional motion of the PNC and the random movement of a much smaller MTOC center that is likely not rigidly attached to the pronucleus.

For a given total amount of force, the rod could experience both translational and rotational motion, due to the torque component of the forces. In the high-viscosity environment we examined here, the angular velocities were proportional to net force as follows:

$$\mu \frac{d\theta_0}{dt} = r_p \left(\vec{e}_0 \times \vec{F}_1 + \vec{e}_0 \times \vec{F}_2\right), \text{rotational motion} \tag{5}$$

where μ is the rotational drag coefficient.

Parameter values

Parameter values used in this investigation are given in Table 1. Where possible, values derived from the experimental literature were used. In the absence of in vivo measurements, we estimated the probability of an MT having a productive interaction with dynein in a particular region of the cortex. In the posterior, we assumed this probability was $P_p = 1.0$ so that, if a dynein was available, it would interact with an MT that contacted the cortex. In the anterior, we assumed this probability was $P_a = 0.65$, reflecting a reduction in cortical pulling forces in the anterior despite no change in individual dynein pulling forces (Grill *et al.*, 2001, 2003; Kotak *et al.*, 2012). While the attachment of the MT to the dynein has a force–velocity relation, it is likely that the actomyosin dynamics might affect these relations in nontrivial ways; in the interest of simplicity, we opted to fix the dynein pulling forces to values corresponding to motor stall forces. A similar approximation was applied to polymerization ratcheting forces.

The approximate range of the translational drag coefficient η for the PNC was estimated using the Stokes's law, which gives the drag coefficient for a spherical object moving in viscous fluid with $\eta = 6\pi r_p a$, where r_p corresponds to the radius of the PNC, and *a* is the fluid viscosity. The optimal rotational drag coefficient μ was ~100 times greater than translational drag, due to the large size of the MT array.

The rest of the parameter values were obtained from the literature and optimized within published ranges in the parameter studies in our correlation and sensitivity analysis, as detailed below.

Model implementation

We numerically integrated the system of equations using the explicit Euler-Maruyama approximation scheme (Kloeden *et al.*, 2003).

Model criteria	Description
Reasonable solutions	Simulations complete without errors and produce real valued solutions.
Centration	The *x* position at the end of the time course must be between ±5 μm, and the *y* position must be between ±1 μm from the center.
Rotation	The angle of the PNC at the end of the time course must be < 20° from horizontal.
y Excursion	The *y* position must not exceed ±2 μm from the *x*-axis at any time during the simulation, based on measurements from live embryos (not shown).
Timing	Centration must be faster than rotation (see Figures 1D and 6A for illustration).
Minimum MT density	The ratio of the number of MTs to the size of the MT array must be greater than 8.3 (N_{MT1}/*arrayRange1* > 8.3; see Figure 5F). This is to ensure that, when the *arrayRange* of MTOC1 is increased, the MT number nucleated at MTOC1 must also increase to maintain an MT density at least as large as MTOC2 has.
Minimum LET-99 band size	The arc length of the LET-99 band must be at least 7.4 μm (s > 3.7 μm; Supplemental Figure S1). By setting this requirement according to our experimental data, we are assuming there is a minimum region of the cortex, ~10–15% EL in which dynein is completely inhibited (Rose and Kemphues, 1998).

TABLE 2: Criteria used to determine whether model behavior matched experimentally observed behavior in our parameter search.

The time step of the simulation, τ, was chosen to be much smaller than any of the reaction timescales in the model.

Microtubule catastrophe/rescue events were captured by stochastic simulation of Poisson processes, with distributions corresponding to catastrophe/rescue frequencies of MTs. For example, for a growing MT with a catastrophe frequency k_c, in the simulation time τ, the probability of the MT switching to a shortening state was $p_i = 1 - e^{(-k_c \tau)}$. Using a standard Monte Carlo technique, we decided whether this transition occurred, that is, a uniform random number *rand* is drawn from the unit interval, and if $p_i > r \in U[0,1]$, catastrophe occurred, and the MT was shortened with rate v_s. Once an MT was detected at the cell cortex, a connection with a dynein in a pull region occurred with probability P_a or P_p, denoting the anterior or posterior of the cell, respectively. The MT could connect with the dynein anywhere in the pull region *k*, and any subsequent MT making a connection in region *k* had probability $P = 0$ of connecting with dynein. Instead, a pushing force was generated from the rest of these MTs. Connection times for either dynein-connected or pushing MTs was decided based on prescribed detachment rates and optimization in our parameter search. If multiple MTs reached the same cortical region at the same time, then we used the Monte Carlo technique to decide whether dynein binding occurred, and then one of the MTs was randomly chosen to connect. Finally, the net force on the PNC was computed as the total sum of forces from cortically connected MTs (Eq. 2).

While we restricted MT nucleation using the parameter *arrayRangei*, *i* = 1, 2, the size of the MT array was necessarily dynamic during a simulation, when the PNC rotated as a result of multiple MT–cortex interactions. In particular, a new MT could only be nucleated at an angle contained in the range specified by the MT *arrayRangei* parameter. An MT could easily fall outside this *arrayRangei* if the PNC rotated and the MT was still attached at a pulling point on the cortex. To address this, we allowed cortically attached MTs to experience some stretch when the PNC rotated. If the PNC rotated, we allowed for the unattached MTs to also rotate, since they were assumed to be rigidly connected to the MTOC. Finally, an MT that fell outside the allowed angle once it was released from the cortex was immediately removed from the simulation, unless it was sitting within 9° of its *arrayRangei*. Any MTs that are left outside the *arrayRangei* likely lose contact with the MTOC and quickly catastrophe, which we simplify by assuming rapid removal. In vivo, the dynamics of MT array rotation are likely more complex. While our in vivo measurements suggested that the nucleation angle varied over time (Figure 5), for simplicity, we assumed *arrayRangei* did not vary over the course of the simulation and used a time-averaged value.

Correlation and sensitivity analysis

To determine relationships between model properties and between the parameters themselves, we conducted correlation (Marino *et al.*, 2008; Gomero, 2012) and sensitivity (Saltelli and Annoni, 2010; Anderson *et al.*, 2014) analyses.

We used Latin hypercube sampling with nonreplacement to generate the 16,000 parameter sets analyzed here. The 14 parameters varied in the 16,000 parameter sets are indicated by a superscript "c" in Table 1, along with their sampling ranges. The sampling range was determined by taking a parameter set that closely approximated the appropriate model behavior and then varying the chosen parameters by ±50%. Given the large number of possible parameter sets with 14 independently varying parameters, approximately $(1000!)^{13}$ for Latin hypercube sampling with 1000 divisions and 14 variables (Stein, 1987), it is not feasible to sample all possible parameter combinations. However, visual inspection of the distribution of parameter values suggests that the 16,000 sets tested are evenly distributed throughout parameter space. Of the 85 sets that satisfied the strict criteria specified in Table 2 (reasonable solutions, centration, rotation, *y* excursion, timing, minimum MT density, and minimum LET-99 band size), we chose one reference set for further simulations. These reference parameter values are listed in Table 1 as "Simulation Parameters." The correlation analysis was performed

Model output	Description
Time to initiate rotation	The first time point where the PNC rotates a minimum of 10°
Time to center	The first time point where the PNC reaches an *x* position of 5 μm
Time to finish rotation	The first time point where the PNC rotates to within 20° of horizontal
Final *x* position	The mean *x* position of the final 10 time points

TABLE 3: Model outputs that correlated with parameter values in Supplemental Figure S5.

on all 16,000 randomly generated sets by quantifying relationships between parameter values and model outputs, which are listed in Table 3. The sensitivity analysis was performed by selecting specific parameters for further analysis, and quantifying model outputs, specifically final orientation and *x* position of the PNC.

ACKNOWLEDGMENTS

This work is supported by NIH postdoctoral F32 fellowship GM110977 and a Pelotonia Fellowship Program postdoctoral fellowship awarded to V.C.C., Pomona College Startup Funds and National Science Foundation (NSF) grant DMS-1358932 to B.S., and NSF/NIH grant DMS/NIGMS-1361251 and NSF grant DMS-1554896 to A.T.D. Any opinions, findings, and conclusions expressed in this material are those of the authors and do not necessarily reflect those of the Pelotonia Fellowship Program.

REFERENCES

Anderson B, Borgonovo E, Galeotti M, Roson R (2014). Uncertainty in climate change modeling: can global sensitivity analysis be of help? Risk Anal 34, 271–293.

Bettencourt-Dias M, Hildebrandt F, Pellman D, Woods G, Godinho SA (2011). Centrosomes and cilia in human disease. Trends Genet 27, 307–315.

Bringmann H, Cowan CR, Kong J, Hyman AA (2007). LET-99, GOA-1/GPA-16, and GPR-1/2 are required for aster-positioned cytokinesis. Curr Biol 17, 185–191.

Brunner D, Nurse P (2000). CLIP170-like tip1p spatially organizes microtubular dynamics in fission yeast. Cell 102, 695–704.

Cassimeris L, Pryer NK, Salmon E (1988). Real-time observations of microtubule dynamic instability in living cells. J Cell Biol 107, 2223–2231.

Coffman VC, Wu P, Parthun MR, Wu JQ (2011). CENP-A exceeds microtubule attachment sites in centromere clusters of both budding and fission yeast. J Cell Biol 195, 563–572.

Daniels BR, Masi BC, Wirtz D (2006). Probing single-cell micromechanics in vivo: the microrheology of *C. elegans* developing embryos. Biophys J 90, 4712–4719.

Decker M, Jaensch S, Pozniakovsky A, Zinke A, O'Connell KF, Zachariae W, Myers E, Hyman AA (2011). Limiting amounts of centrosome material set centrosome size in *C. elegans* embryos. Curr Biol 21, 1259–1267.

DeSimone A, Nédélec F, Gönczy P (2016). Dynein transmits polarized actomyosin cortical flows to promote centrosome separation. Cell Rep 14, 2250–2262.

Dogterom M, Kerssemakers JW, Romet-Lemonne G, Janson ME (2005). Force generation by dynamic microtubules. Curr Opin Cell Biol 17, 67–74.

Dogterom M, Yurke B (1997). Measurement of the force-velocity relation for growing microtubules. Science 278, 856–860.

Engel BD, Ludington WB, Marshall WF (2009). Intraflagellar transport particle size scales inversely with flagellar length: revisiting the balance-point length control model. J Cell Biol 187, 81–89.

Etemad-Moghadam B, Guo S, Kemphues KJ (1995). Asymmetrically distributed PAR-3 protein contributes to cell polarity and spindle alignment in early *C. elegans* embryos. Cell 83, 743–752.

Goldstein B, Hird SN (1996). Specification of the anteroposterior axis in *Caenorhabditis elegans*. Development 122, 1467–1474.

Gomero B (2012). Latin hypercube sampling and partial rank correlation coefficient analysis applied to an optimal control problem. Master's Thesis. Knoxville: University of Tennessee.

Gönczy P, Pichler S, Kirkham M, Hyman AA (1999). Cytoplasmic dynein is required for distinct aspects of MTOC positioning, including centrosome separation, in the one cell stage *Caenorhabditis elegans* embryo. J Cell Biol 147, 135–150.

Grill SW, Gönczy P, Stelzer EHK, Hyman AA (2001). Polarity controls forces governing asymmetric spindle positioning in the *Caenorhabditis elegans* embryo. Nature 409, 630–633.

Grill SW, Howard J, Schäffer E, Stelzer EH, Hyman AA (2003). The distribution of active force generators controls mitotic spindle position. Science 301, 518–521.

Grill SW, Hyman AA (2005). Spindle positioning by cortical pulling forces. Dev Cell 8, 461–465.

Gross SP, Welte MA, Block SM, Wieschaus EF (2000). Dynein-mediated cargo transport in vivo: a switch controls travel distance. J Cell Biol 148, 945–956.

Guo S, Kemphues KJ (1995). *par-1*, a gene required for establishing polarity in *C. elegans* embryos, encodes a putative Ser/Thr kinase that is asymmetrically distributed. Cell 81, 611–620.

Hannak E, Oegema K, Kirkham M, Gönczy P, Habermann B, Hyman AA (2002). The kinetically dominant assembly pathway for centrosomal asters in *Caenorhabditis elegans* is γ-tubulin dependent. J Cell Biol 157, 591–602.

Hyman AA, White JG (1987). Determination of cell division axes in the early embryogenesis of *Caenorhabditis elegans*. J Cell Biol 105, 2123–2135.

Janson ME, Dogterom M (2004). Scaling of microtubule force-velocity curves obtained at different tubulin concentrations. Phys Rev Lett 92, 248101.

Kemphues KJ, Priess JR, Morton DG, Cheng NS (1988). Identification of genes required for cytoplasmic localization in early *C. elegans* embryos. Cell 52, 311–320.

Kimura K, Kimura A (2011). Intracellular organelles mediate cytoplasmic pulling force for centrosome centration in the *Caenorhabditis elegans* early embryo. Proc Natl Acad Sci USA 108, 137–142.

Kimura A, Onami S (2005). Computer simulations and image processing reveal length-dependent pulling force as the primary mechanism for *C. elegans* male pronuclear migration. Dev Cell 8, 765–775.

Kimura A, Onami S (2007). Local cortical pulling-force repression switches centrosomal centration and posterior displacement in *C. elegans*. J Cell Biol 179, 1347–1354.

Kirkham M, Müller-Reichert T, Oegema K, Grill S, Hyman AA (2003). SAS-4 is a *C. elegans* centriolar protein that controls centrosome size. Cell 112, 575–587.

Kloeden PE, Platen E, Schurz H (2003). Numerical Solution of SDE through Computer Experiments, 3rd ed., Heidelberg, Germany: Universitext Springer-Verlag.

Kotak S, Busso C, Gönczy P (2012). Cortical dynein is critical for proper spindle positioning in human cells. J Cell Biol 199, 97–110.

Kozlowski C, Srayko M, Nédélec F (2007). Cortical microtubule contacts position the spindle in *C. elegans* embryos. Cell 129, 499–510.

Krueger LE, Wu JC, Tsou MFB, Rose LS (2010). LET-99 inhibits lateral posterior pulling forces during asymmetric spindle elongation in *C. elegans* embryos. J Cell Biol 189, 481–495.

Laan L, Pavin N, Husson J, Romet-Lemonne G, Van Duijn M, López MP, Vale RD, Jülicher F, Reck-Peterson SL, Dogterom M (2012). Cortical dynein controls microtubule dynamics to generate pulling forces that position microtubule asters. Cell 148, 502–514.

Labbé JC, Maddox PS, Salmon ED, Goldstein B (2003). PAR proteins regulate microtubule dynamics at the cell cortex in *C. elegans*. Curr Biol 13, 707–714.

Labbé JC, McCarthy EK, Goldstein B (2004). The forces that position a mitotic spindle asymmetrically are tethered until after the time of spindle assembly. J Cell Biol 167, 245–256.

Leake MC, Chandler JH, Wadhams GH, Bai F, Berry RM, Armitage JP (2006). Stoichiometry and turnover in single, functioning membrane protein complexes. Nature 443, 355–358.

Mallik R, Carter BC, Lex SA, King SJ, Gross SP (2004). Cytoplasmic dynein functions as a gear in response to load. Nature 427, 649–652.

Malone CJ, Misner L, Le Bot N, Tsai MC, Campbell JM, Ahringer J, White JG (2003). The *C. elegans* hook protein, ZYG-12, mediates the essential attachment between the centrosome and nucleus. Cell 115, 825–836.

Marino S, Hogue IB, Ray CJ, Kirschner DE (2008). A methodology for performing global uncertainty and sensitivity analysis in systems biology. J Theor Biol 254, 178–196.

Marumoto T, Zhang D, Saya H (2005). Aurora-A—a guardian of poles. Nat Rev Cancer 5, 42–50.

Minn IL, Rolls MM, Hanna-Rose W, Malone CJ (2009). SUN-1 and ZYG-12, mediators of centrosome-nucleus attachment, are a functional SUN/KASH pair in *Caenorhabditis elegans*. Mol Biol Cell 20, 4586–4595.

Mitchison T, Kirschner M (1984). Dynamic instability of microtubule growth. Nature 312, 237–242.

O'Connell KF, Maxwell KN, White JG (2000). The *spd-2* gene is required for polarization of the anteroposterior axis and formation of the sperm asters in the *Caenorhabditis elegans* zygote. Dev Biol 222, 55–70.

Peskin CS, Odell GM, Oster GF (1993). Cellular motions and thermal fluctuations: the Brownian ratchet. Biophys J 65, 316–324.

Rose LS, Kemphues K (1998). The *let-99* gene is required for proper spindle orientation during cleavage of the *C. elegans* embryo. Development 125, 1337–1346.

Saltelli A, Annoni P (2010). How to avoid a perfunctory sensitivity analysis. Environ Model Softw 25, 1508–1517.
Shinar T, Mana M, Piano F, Shelley MJ (2011). A model of cytoplasmically driven microtubule-based motion in the single-celled *Caenorhabditis elegans* embryo. Proc Natl Acad Sci USA 108, 10508–10513.
Spiró Z, Thyagarajan K, DeSimone A, Träger S, Afshar K, Gönczy P (2014). Clathrin regulates centrosome positioning by promoting acto-myosin cortical tension in *C. elegans* embryos. Development 141, 2712–2723.
Srayko M, Kaya A, Stamford J, Hyman AA (2005). Identification and characterization of factors required for microtubule growth and nucleation in the early *C. elegans* embryo. Dev Cell 9, 223–236.
Stein M (1987). Large sample properties of simulations using Latin hypercube sampling. Technometrics 29, 143–151.
Tsou MFB, Hayashi A, DeBella LR, McGrath G, Rose LS (2002). LET-99 determines spindle position and is asymmetrically enriched in response to PAR polarity cues in *C. elegans* embryos. Development 129, 4469–4481.
Tsou MFB, Ku W, Hayashi A, Rose LS (2003). PAR-dependent and geometry-dependent mechanisms of spindle positioning. J Cell Biol 160, 845–855.
Wallenfang MR, Seydoux G (2000). Polarization of the anterior-posterior axis of *C. elegans* is a microtubule-directed process. Nature 408, 89–92.
Walston T, Hardin J (2010). An agar mount for observation of *Caenorhabditis elegans* embryos. Cold Spring Harb Protoc 2010, pdb.prot5540.
Watts JL, Etemad-Moghadam B, Guo S, Boyd L, Draper BW, Mello CC, Priess JR, Kemphues KJ (1996). *par-6*, a gene involved in the establishment of asymmetry in early *C. elegans* embryos, mediates the asymmetric localization of PAR-3. Development 122, 3133–3140.
Zwicker D, Decker M, Jaensch S, Hyman AA, Jülicher F (2014). Centrosomes are autocatalytic droplets of pericentriolar material organized by centrioles. Proc Natl Acad Sci USA 111, E2636–E2645.